HOSTED BY

ELSEVIER

Available online at www.sciencedirect.com

ScienceDirect

Journal of Computational Design and Engineering 2 (2015) 233–247

www.elsevier.com/locate/jcde

A combination method of the theory and experiment in determination of cutting force coefficients in ball-end mill processes

Yung-Chou Kao[a], Nhu-Tung Nguyen[b,*], Mau-Sheng Chen[b], Shyh-Chour Huang[b]

[a]*Advanced Institute of Manufacturing with Hi-tech Innovations, National Chung Cheng University, 621 Taiwan, ROC*
[b]*Department of Mechanical Engineering, National Kaohsiung University of Applied Sciences, 807 Taiwan, ROC*

Received 15 February 2015; received in revised form 26 May 2015; accepted 10 June 2015
Available online 23 June 2015

Abstract

In this paper, the cutting force calculation of ball-end mill processing was modeled mathematically. All derivations of cutting forces were directly based on the tangential, radial, and axial cutting force components. In the developed mathematical model of cutting forces, the relationship of average cutting force and the feed per flute was characterized as a linear function. The cutting force coefficient model was formulated by a function of average cutting force and other parameters such as cutter geometry, cutting conditions, and so on. An experimental method was proposed based on the stable milling condition to estimate the cutting force coefficients for ball-end mill. This method could be applied for each pair of tool and workpiece. The developed cutting force model has been successfully verified experimentally with very promising results.

Keywords: Ball-end mill; Cutting force coefficients; Cutting force simulation

1. Introduction

The mechanics of metal-cutting had been analyzed and investigated by orthogonal and oblique models in many works such as Merchant [1] and Altintas [2]. In the prediction of cutting forces, there are significant differences in the approach used in implementing the models. Traditionally, the cutting forces were modeled based on the experiential chip-force relationship according to cutting force coefficients. Therefore, effective methods for calibrating the cutting coefficients are the important keys to model the cutting forces in machining processes.

In the conventional mechanistic approach, the cutting force coefficients were calibrated for different pairs of tool and workpiece through the cutting tests. There are two typical methods for the calibration of cutting force coefficients. The first method is the orthogonal to the oblique cutting transformation method and the second method is the direct calibration method. In the first method, the cutting force coefficients were determined by using the shear angle, friction angle, and shear yield stress resulted from orthogonal cutting tests. By using this approach, in the flat-end mill, the cutting force coefficients were determined using the oblique cutting model, the orthogonal cutting model, and the cutting data [2–4]. Besides, by using the calculated results of shear angle, friction angle, and shear yield stress from orthogonal cutting and using the orthogonal and oblique cutting models, some researchers had developed the cutting models to calculate the cutting force coefficients in ball-end milling operations [5–7].

In the second method, the cutting force coefficients were estimated directly from milling tests for the specific cutter part combination. The cutting force coefficients were determined based on the instantaneous uncut chip thickness, the cutting edge

*Corresponding author.
E-mail address: tungdhhv@gmail.com (N.-T. Nguyen).
Peer review under responsibility of Society of CAD/CAM Engineers.

http://dx.doi.org/10.1016/j.jcde.2015.06.005

Nomenclature

D	the diameter of cutter [mm]
R_0	the diameter of cutter [mm]
N_f	the number of flutes on the cutter
β	the helix angle on the cutter [deg]
ϕ_P	the cutter pitch angle [deg]
a	the full axial depth of cut [mm]
dz	the differential axial depth of cut [mm]
$\Psi(\phi_j(z))$	the lag angle at an axial depth of cut z [deg]
Ψ_0	the lag angle at maximum axial depth of cut $z=a$ [deg]
ϕ_j	the instantaneous immersion angle of flute number j, ($j = 1$–N_f) [deg]
$\phi_j(z)$	the instantaneous immersion angle of flute number j in z cutting depth, ($j = 1$–N_f) [deg]
$h_j(\phi_j(z))$	the instantaneous chip thickness at immersion angle ϕ_j [mm]
db	the chip width [mm]
dS	the edge length of the cutting segment [mm]
$r(\phi_j(z))$	the radius of a circle on xy plane at an arbitrary point (P) on cutting edge [mm]
f_t	the feed per tooth [mm/tooth]
$\kappa(z)$	the axial immersion angle at z axial depth of cut
K_{tc}	tangential shearing force coefficient [N/mm^2]
K_{rc}	radial shearing force coefficient [N/mm^2]
K_{ac}	axial shearing force coefficient [N/mm^2]
K_{te}	tangential edge force coefficient [N/mm]
K_{re}	radial edge force coefficient [N/mm]
K_{ae}	axial edge force coefficient [N/mm]
$dF_{t,j}(\phi,z)$	the differential tangential cutting force [N]
$dF_{r,j}(\phi,z)$	the differential radial cutting force [N]
$dF_{a,j}(\phi,z)$	the differential axial cutting force [N]
$dF_{f,j}(\phi,z)$	the differential feed cutting force [N]
$dF_{n,j}(\phi,z)$	the differential normal cutting force [N]
$F_f(\phi)$	the cutting force in the feed direction [N]
$F_n(\phi)$	the cutting force in the normal direction [N]
$F_a(\phi)$	the cutting force in the axial direction [N]
$\overline{F}_f$	the average cutting force in the feed direction [N]
$\overline{F}_{fc}, \overline{F}_{fe}$	the components of linear model force in the feed direction [N]
$\overline{F}_n$	the average cutting force in the normal direction [N]
$\overline{F}_{nc}, \overline{F}_{ne}$	the components of linear model force in the normal direction [N]
$\overline{F}_a$	the average cutting force in the axial direction [N]
$\overline{F}_{ac}, \overline{F}_{ae}$	the components of linear model force in the axial direction [N]

length, and the spindle speed [8]. By considering the instantaneous uncut chip thickness and the cutter rake angle simultaneously, Bayoumi et al. [9] had successfully determined the cutting force coefficients. Shin and Waters [10] developed a model to estimate the cutting force coefficients with an improved simulation model of chip flow angle. In this study, the instantaneous cutting force coefficients were directly determined from experiments with variations of feedrate and depth of cut. In milling processes, the effect of cutting forces will deflect the tool. And with the deflection and rotation of the tool, the finished surface was created. Larue and Anselmetti [11] used the relationship between finished surface (tool deflection) and cutting forces to determine the cutting force coefficients in flank milling. The cutting force coefficients were estimated by using the relationship between the instantaneous uncut chip thickness and the instantaneous cutting forces [12]. Subrahmanyam et al. [13] used the corresponding maximum chip area and maximum measured force to estimate the cutting force coefficients. Besides, the cutting force coefficients were determined by using the relationship between measured average cutting force and the feedrate [14–16].

The linear model of average cutting force and feed per flute was used to calculate the cutting force coefficients for milling process in the direct calibration method. In this model, the cutting force coefficients were relatively dependent on the average cutting force and were determined from experimental data. This model had been applied in milling tools of flat-end mill [14–19], ball-end mill [20], and bull-end mill [21]. However, it seems that when determining the cutting force coefficients in the ball-end mill process, the application of cutting conditions have not been evaluated, the linear model of average cutting force and feed per flute has also not been verified; This means there still exist issues affecting the calculation of cutting force coefficients to be resolved.

In this study, the cutting force coefficients were estimated from the experimental data of cutting forces in the stable cutting conditions. The main contributions of this study lie in four aspects: (1) completing the method to determine the cutting force coefficients in the ball-end mill, (2) using the experimental method to determine the stable cutting conditions, (3) verifying the linear model of average cutting force and feed per flute was verified by experimental results, and (4) modeling and verifying the cutting forces in the ball-end mill processes.

2. Mathematics of cutting force model for ball-end mill

2.1. The cutting force model

In ball-end mill, the immersion is measured clockwise from the normal axis. Assuming that the bottom end of flute number one is designated as the reference immersion angle (ϕ_1) and the bottom end point of the remaining flute number j is at an angle (ϕ_j), as

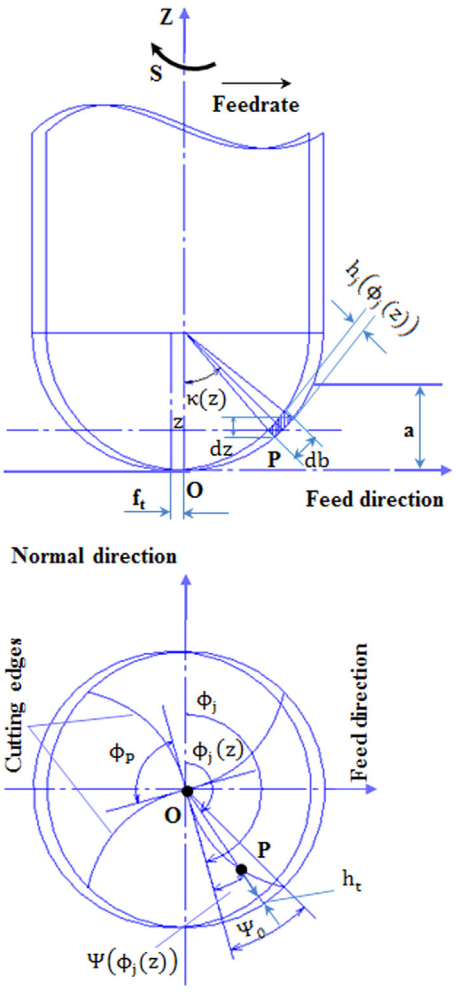

Fig. 1. The angular position of the cutter's flute.

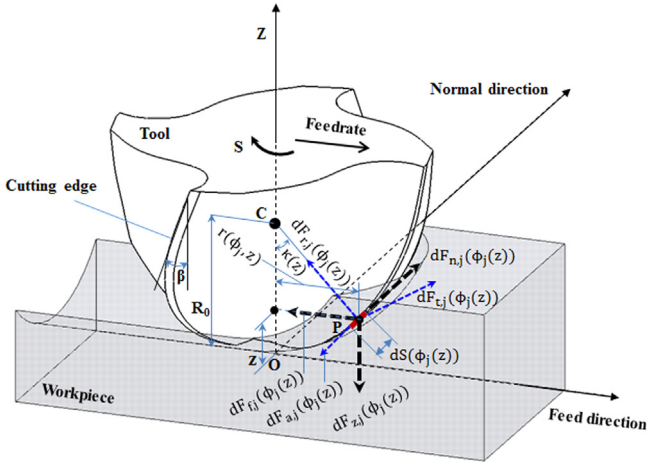

Fig. 2. Geometry of ball-end mill cutter and milling process.

shown in Fig. 1 and Fig. 2, then ϕ_j can be expressed as in Eq. (1).

$$\phi_j = \phi_1 - (j-1)\phi_P, \quad j = 1\text{–}N_f \tag{1}$$

where ϕ_P is the cutter pitch angle that is the lag angle from the flute number j to the flute number $j+1$.

$$\phi_P = \frac{2\pi}{N_f} \tag{2}$$

When considering the cutter's helix angle, the radial lag angle Ψ at each axial depth of cut z can be expressed in Eq. (3).

$$\Psi(\phi_j(z)) = \frac{2\tan\beta}{D} z = \frac{\tan\beta}{R_0} z \tag{3}$$

The maximum radial lag angle Ψ_0 is determined at maximum depth of cut a, and can be determined by Eq. (4)

$$\Psi_0 = \frac{\tan\beta}{R_0} a \tag{4}$$

For flute number j, at an axial depth of cut z, the immersion angle is $\phi_j(z)$. It can be expressed by Eq. (5), as shown in Fig. 1.

$$\phi_j(z) = \phi_j - \Psi(\phi_j(z)) = \phi_j - \frac{\tan\beta}{R_0} z \tag{5}$$

If zero nose radius of the cutter is assumed, the tangential, radial, and axial forces acting on a differential flute element can be expressed as in Eq. (6).

$$\begin{cases} dF_{t,j}(\phi_j(z)) = K_{tc} * h_j(\phi_j(z)) * db + K_{te} * dS(\phi_j(z)) \\ dF_{r,j}(\phi_j(z)) = K_{rc} * h_j(\phi_j(z)) * db + K_{re} * dS(\phi_j(z)) \\ dF_{a,j}(\phi_j(z)) = K_{ac} * h_j(\phi_j(z)) * db + K_{ae} * dS(\phi_j(z)) \end{cases} \tag{6}$$

where $h_j(\phi_j(z))$ is the instantaneous chip thickness, db is the chip width, dS is the edge length of the cutting segment that are explained in the Appendix section.

In Figs. 1 and 2, each point at cutting edge is determined by z coordinate and the angular position (ϕ_j). In those points, the cutting forces consist of three components including radial force, tangential force, and axial force. The feed direction is the direction that is parallel to the tool movement direction, and perpendicular to the tool axis. The normal direction is perpendicular to the tool movement direction and tool axis. The axial direction is parallel to the tool axis and perpendicular to the tool path. So, the elemental forces in feed, normal, and axial force are calculated by using the transformation as in Eq. (7).

$$\begin{Bmatrix} dF_{f,j}(\phi_j(z)) \\ dF_{n,j}(\phi_j(z)) \\ dF_{z,j}(\phi_j(z)) \end{Bmatrix} = \begin{bmatrix} -\cos(\phi_j(z)) & -\sin(\kappa(z))\sin(\phi_j(z)) & -\cos(\kappa(z))\sin(\phi_j(z)) \\ \sin(\phi_j(z)) & -\sin(\kappa(z))\cos(\phi_j(z)) & -\cos(\kappa(z))\cos(\phi_j(z)) \\ 0 & \cos(\kappa(z)) & -\sin(\kappa(z)) \end{bmatrix} \begin{Bmatrix} dF_{t,j}(\phi_j(z)) \\ dF_{r,j}(\phi_j(z)) \\ dF_{a,j}(\phi_j(z)) \end{Bmatrix} \tag{7}$$

where $\kappa(z)$ is the axial immersion angle at z axial depth of cut that is explained in the Appendix section.

By substituting Eq. (5) into Eq. (7), the elemental forces in feed, normal, and axial force are calculated by Eq. (8) to Eq. (11).

$$\begin{Bmatrix} dF_{f,j}(\phi_j(z)) \\ dF_{n,j}(\phi_j(z)) \\ dF_{a,j}(\phi_j(z)) \end{Bmatrix} = \begin{bmatrix} -\cos\left(\phi_j - \frac{\tan\beta}{R_0} z\right) & -\sin(\kappa(z))\sin\left(\phi_j - \frac{\tan\beta}{R_0} z\right) & -\cos(\kappa(z))\sin\left(\phi_j - \frac{\tan\beta}{R_0} z\right) \\ \sin\left(\phi_j - \frac{\tan\beta}{R_0} z\right) & -\sin(\kappa(z))\cos\left(\phi_j - \frac{\tan\beta}{R_0} z\right) & -\cos(\kappa(z))\cos\left(\phi_j - \frac{\tan\beta}{R_0} z\right) \\ 0 & \cos(\kappa(z)) & -\sin(\kappa(z)) \end{bmatrix} \begin{Bmatrix} dF_{t,j}(\phi_j(z)) \\ dF_{r,j}(\phi_j(z)) \\ dF_{a,j}(\phi_j(z)) \end{Bmatrix} \tag{8}$$

and

$$\begin{cases} dF_{f,j}(\phi_j(z)) = -\cos\left(\phi_j - \frac{\tan\beta}{R_0} z\right) dF_{t,j}(\phi_j(z)) - \sin(\kappa(z))\sin\left(\phi_j - \frac{\tan\beta}{R_0} z\right) dF_{r,j}(\phi_j(z)) \\ -\cos(\kappa(z))\sin\left(\phi_j - \frac{\tan\beta}{R_0} z\right) dF_{a,j}(\phi_j(z)) \\ dF_{n,j}(\phi_j(z)) = \sin\left(\phi_j - \frac{\tan\beta}{R_0} z\right) dF_{t,j}(\phi_j(z)) - \sin(\kappa(z))\cos\left(\phi_j - \frac{\tan\beta}{R_0} z\right) dF_{r,j}(\phi_j(z)) \\ -\cos(\kappa(z))\cos\left(\phi_j - \frac{\tan\beta}{R_0} z\right) dF_{a,j}(\phi_j(z)) \\ dF_{a,j}(\phi_j(z)) = \cos(\kappa(z)) dF_{r,j}(\phi, z) - \sin(\kappa(z)) dF_{a,j}(\phi_j(z)) \end{cases} \tag{9}$$

and

$$\begin{cases} \mathrm{d}F_{f,j}(\phi_j(z)) = -\cos\left(\phi_j - \frac{\tan\beta}{R_0}z\right)\left[K_{tc}*f_t\ \sin\left(\phi_j - \frac{\tan\beta}{R_0}z\right) + K_{te}*M\right]\mathrm{d}z \\ -\sin(\kappa(z))\ \sin\left(\phi_j - \frac{\tan\beta}{R_0}z\right)\left[K_{rc}*f_t\ \sin\left(\phi_j - \frac{\tan\beta}{R_0}z\right) + K_{re}*M\right]\mathrm{d}z \\ -\cos(\kappa(z))\ \sin\left(\phi_j - \frac{\tan\beta}{R_0}z\right)\left[K_{ac}*f_t\ \sin\left(\phi_j - \frac{\tan\beta}{R_0}z\right) + K_{ae}*M\right]\mathrm{d}z \\ \mathrm{d}F_{n,j}(\phi_j(z)) = \sin\left(\phi_j - \frac{\tan\beta}{R_0}z\right)\left[K_{tc}*f_t\ \sin\left(\phi_j - \frac{\tan\beta}{R_0}z\right) + K_{te}*M\right]\mathrm{d}z \\ -\sin(\kappa(z))\ \cos\left(\phi_j - \frac{\tan\beta}{R_0}z\right)\left[K_{rc}*f_t\ \sin\left(\phi_j - \frac{\tan\beta}{R_0}z\right) + K_{re}*M\right]\mathrm{d}z \\ -\cos(\kappa(z))\ \cos\left(\phi_j - \frac{\tan\beta}{R_0}z\right)\left[K_{ac}*f_t\ \sin\left(\phi_j - \frac{\tan\beta}{R_0}z\right) + K_{ae}*M\right]\mathrm{d}z \\ \mathrm{d}F_{a,j}(\phi_j(z)) = \cos(\kappa(z))\left[K_{rc}*f_t\ \sin\left(\phi_j - \frac{\tan\beta}{R_0}z\right) + K_{re}*M\right]\mathrm{d}z \\ -\sin(\kappa(z))\left[K_{ac}*f_t\ \sin\left(\phi_j - \frac{\tan\beta}{R_0}z\right) + K_{ae}*M\right]\mathrm{d}z \end{cases} \tag{10}$$

So,

$$\begin{cases} \mathrm{d}F_{f,j}(\phi_j(z)) = \begin{pmatrix} K_{tc}*f_t\left[-\cos\left(\phi_j - \frac{\tan\beta}{R_0}z\right)\sin\left(\phi_j - \frac{\tan\beta}{R_0}z\right)\right] \\ +K_{te}\left[-\cos\left(\phi_j - \frac{\tan\beta}{R_0}z\right)*M\right] \\ +K_{rc}*f_t\left[-\sin(\kappa(z))\ \sin^2\left(\phi_j - \frac{\tan\beta}{R_0}z\right)\right] \\ +K_{re}\left[-\sin(\kappa(z))\ \sin\left(\phi_j - \frac{\tan\beta}{R_0}z\right)*M\right] \\ +K_{ac}*f_t\left[-\cos(\kappa(z))\ \sin^2\left(\phi_j - \frac{\tan\beta}{R_0}z\right)\right] \\ +K_{ac}*f_t\left[-\cos(\kappa(z))\ \sin^2\left(\phi_j - \frac{\tan\beta}{R_0}z\right)\right] \end{pmatrix}\mathrm{d}z \\ \mathrm{d}F_{n,j}(\phi_j(z)) = \begin{pmatrix} K_{tc}*f_t\left[\sin^2\left(\phi_j - \frac{\tan\beta}{R_0}z\right)\right] \\ +K_{te}\left[\sin\left(\phi_j - \frac{\tan\beta}{R_0}z\right)*M\right] \\ +K_{rc}*f_t\left[-\sin(\kappa(z))\ \sin\left(\phi_j - \frac{\tan\beta}{R_0}z\right)\cos\left(\phi_j - \frac{\tan\beta}{R_0}z\right)\right] \\ +K_{re}\left[-\sin(\kappa(z))\cos\left(\phi_j - \frac{\tan\beta}{R_0}z\right)*M\right] \\ +K_{ac}*f_t\left[-\cos(\kappa(z))\ \sin\left(\phi_j - \frac{\tan\beta}{R_0}z\right)\cos\left(\phi_j - \frac{\tan\beta}{R_0}z\right)\right] \\ +K_{ae}\left[-\cos(\kappa(z))\cos\left(\phi_j - \frac{\tan\beta}{R_0}z\right)*M\right] \end{pmatrix}\mathrm{d}z \\ \mathrm{d}F_{a,j}(\phi_j(z)) = \begin{pmatrix} K_{rc}*f_t\left[\cos(\kappa(z))\sin\left(\phi_j - \frac{\tan\beta}{R_0}z\right)\right] \\ +K_{re}[\cos(\kappa(z))*M] \\ +K_{ac}*f_t\left[-\sin(\kappa(z))\ \sin\left(\phi_j - \frac{\tan\beta}{R_0}z\right)\right] \\ +K_{ae}[-\sin(\kappa(z))*M] \end{pmatrix}\mathrm{d}z \end{cases} \tag{11}$$

where M is the setting parameter that is calculated by Eq. (A.11) in the Appendix section.

In the determination of the total cutting force, the differential cutting forces are integrated analytically along the in-cut portion of the flute j, Eq. (12).

$$F_q(\phi_j) = \int_{z_1(\phi_j)}^{z_2(\phi_j)} dF_q(\phi_j(z)), \quad q = f, n, a \tag{12}$$

Considering the case that has more than one tooth executing the cutting processes simultaneously, the total cutting forces on the feed, normal, and axial direction can be determined by Eq. (13).

$$F_f(\phi)=\sum_{j=1}^{N_f}F_{f,j}(\phi_j),\quad F_n(\phi)=\sum_{j=1}^{N_f}F_{n,j}(\phi_j),\quad F_a(\phi)=\sum_{j=1}^{N_f}F_{a,j}(\phi_j) \tag{13}$$

2.2. Identification of cutting force coefficients

In feed, normal, and axial direction, the average cutting forces of N_f flutes per revolution can be expressed by Eq. (14).

$$\begin{cases}\overline{F}_f=\frac{N_f}{2\pi}\int_0^{2\pi}\left(\int_{z_2(\phi_j)}^{z_2(\phi_j)}dF_f(\phi_j(z))\right)\mathrm{d}\phi\\ \overline{F}_n=\frac{N_f}{2\pi}\int_0^{2\pi}\left(\int_{z_2(\phi_j)}^{z_2(\phi_j)}dF_n(\phi_j(z))\right)\mathrm{d}\phi\\ \overline{F}_a=\frac{N_f}{2\pi}\int_0^{2\pi}\left(\int_{z_2(\phi_j)}^{z_2(\phi_j)}dF_a(\phi_j(z))\right)\mathrm{d}\phi\end{cases} \tag{14}$$

And then, the Eq. (14) can be rewritten by Eq. (15) to Eq. (19) in feed direction, normal direction, and axial direction as followings:

In feed direction

$$\overline{F}_f=\frac{N_f}{2\pi}\int_0^{2\pi}\left(\int_{z_2(\phi_j)}^{z_2(\phi_j)}\left(\begin{array}{l}K_{tc}*f_t\left[-\cos\left(\phi_j-\frac{\tan\beta}{R_0}z\right)\sin\left(\phi_j-\frac{\tan\beta}{R_0}z\right)\right]\\ \quad+K_{te}\left[-\cos\left(\phi_j-\frac{\tan\beta}{R_0}z\right)*M\right]\\ +K_{rc}*f_t\left[-\sin(\kappa(z))\sin^2\left(\phi_j-\frac{\tan\beta}{R_0}z\right)\right]\\ \quad+K_{re}\left[-\sin(\kappa(z))\sin\left(\phi_j-\frac{\tan\beta}{R_0}z\right)*M\right]\\ +K_{ac}*f_t\left[-\cos(\kappa(z))\sin^2\left(\phi_j-\frac{\tan\beta}{R_0}z\right)\right]\\ \quad+K_{ae}\left[-\cos(\kappa(z))\sin\left(\phi_j-\frac{\tan\beta}{R_0}z\right)*M\right]\end{array}\right)\mathrm{d}z\right)\mathrm{d}\phi \tag{15}$$

so,

$$\overline{F}_f=\frac{N_f}{2\pi}\int_0^{2\pi}\left(\int_{z_2(\phi_j)}^{z_2(\phi_j)}\left(\begin{array}{l}K_{tc}*f_t\left[-\frac{1}{2}\sin\left(2\phi_j-2\frac{\tan\beta}{R_0}z\right)\right]\\ \quad+K_{te}\left[-\cos\left(\phi_j-\frac{\tan\beta}{R_0}z\right)*M\right]\\ +K_{rc}*f_t\left[-\frac{1}{2}\sin(\kappa(z))\left(1-2\cos\left(2\phi_j-2\frac{\tan\beta}{R_0}z\right)\right)\right]\\ \quad+K_{re}\left[-\sin(\kappa(z))\sin\left(\phi_j-\frac{\tan\beta}{R_0}z\right)*M\right]\\ +K_{ac}*f_t\left[-\frac{1}{2}\cos(\kappa(z))\left(1-2\cos\left(2\phi_j-2\frac{\tan\beta}{R_0}z\right)\right)\right]\\ \quad+K_{ae}\left[-\cos(\kappa(z))\sin\left(\phi_j-\frac{\tan\beta}{R_0}z\right)*M\right]\end{array}\right)\mathrm{d}z\right)\mathrm{d}\phi \tag{16}$$

In normal direction

$$\overline{F}_n=\frac{N_f}{2\pi}\int_0^{2\pi}\left(\int_{z_2(\phi_j)}^{z_2(\phi_j)}\left(\begin{array}{l}K_{tc}*f_t\left[\sin^2\left(\phi_j-\frac{\tan\beta}{R_0}z\right)\right]\\ +K_{te}\left[\sin\left(\phi_j-\frac{\tan\beta}{R_0}z\right)*M\right]\\ +K_{rc}*f_t\left[-\sin(\kappa(z))\sin\left(\phi_j-\frac{\tan\beta}{R_0}z\right)\cos\left(\phi_j-\frac{\tan\beta}{R_0}z\right)\right]\\ +K_{re}\left[-\sin(\kappa(z))\cos\left(\phi_j-\frac{\tan\beta}{R_0}z\right)*M\right]\\ +K_{ac}*f_t\left[-\cos(\kappa(z))\sin\left(\phi_j-\frac{\tan\beta}{R_0}z\right)\cos\left(\phi_j-\frac{\tan\beta}{R_0}z\right)\right]\\ +K_{ae}\left[-\cos(\kappa(z))\cos\left(\phi_j-\frac{\tan\beta}{R_0}z\right)*M\right]\end{array}\right)\mathrm{d}z\right)\mathrm{d}\phi \tag{17}$$

so,

$$\overline{F}_n = \frac{N_f}{2\pi}\int_0^{2\pi}\left(\int_{z_2(\phi_j)}^{z_2(\phi_j)}\begin{pmatrix} K_{tc}*f_t\left[\frac{1}{2}\left(1-2\ \cos\left(2\phi_j-2\frac{\tan\beta}{R_0}z\right)\right)\right] \\ +K_{te}\left[\sin\left(\phi_j-\frac{\tan\beta}{R_0}z\right)*M\right] \\ +K_{rc}*f_t\left[-\frac{1}{2}\ \sin(\kappa(z))\ \sin\left(2\phi_j-2\frac{\tan\beta}{R_0}z\right)\right] \\ +K_{re}\left[-\ \sin(\kappa(z))\cos\left(\phi_j-\frac{\tan\beta}{R_0}z\right)*M\right] \\ +K_{ac}*f_t\left[-\frac{1}{2}\ \cos(\kappa(z))\sin\left(2\phi_j-2\frac{\tan\beta}{R_0}z\right)\right] \\ +K_{ae}\left[-\ \cos(\kappa(z))\cos\left(\phi_j-\frac{\tan\beta}{R_0}z\right)*M\right] \end{pmatrix}\mathrm{d}z\right)\mathrm{d}\phi \tag{18}$$

In axial direction

$$\overline{F}_a = \frac{N_f}{2\pi}\int_0^{2\pi}\left(\int_{z_2(\phi_j)}^{z_2(\phi_j)}\begin{pmatrix} K_{rc}*f_t\left[\cos(\kappa(z))\sin\left(\phi_j-\frac{\tan\beta}{R_0}z\right)\right] \\ +K_{re}[\cos(\kappa(z))*M] \\ +K_{ac}*f_t\left[-\ \sin(\kappa(z))\sin\left(\phi_j-\frac{\tan\beta}{R_0}z\right)\right] \\ +K_{ae}[-\ \sin(\kappa(z))*M] \end{pmatrix}\mathrm{d}z\right)\mathrm{d}\phi \tag{19}$$

Setting

$$\begin{cases} C_1 = \frac{N_f}{2\pi}\int_0^{2\pi}\left(\int_{z_2(\phi_j)}^{z_2(\phi_j)}\left[-\frac{1}{2}\ \sin\left(2\phi_j-2\frac{\tan\beta}{R_0}z\right)\right]\mathrm{d}z\right)\mathrm{d}\phi \\ C_2 = \frac{N_f}{2\pi}\int_0^{2\pi}\left(\int_{z_2(\phi_j)}^{z_2(\phi_j)}\left[-\ \cos\left(\phi_j-\frac{\tan\beta}{R_0}z\right)*M\right]\mathrm{d}z\right)\mathrm{d}\phi \\ C_3 = \frac{N_f}{2\pi}\int_0^{2\pi}\left(\int_{z_2(\phi_j)}^{z_2(\phi_j)}\left[-\frac{1}{2}\ \sin(\kappa(z))\ \left(1-2\ \cos\left(2\phi_j-2\frac{\tan\beta}{R_0}z\right)\right)\right]\mathrm{d}z\right)\mathrm{d}\phi \\ C_4 = \frac{N_f}{2\pi}\int_0^{2\pi}\left(\int_{z_2(\phi_j)}^{z_2(\phi_j)}\left[-\ \sin(\kappa(z))\sin\left(\phi_j-\frac{\tan\beta}{R_0}z\right)*M\right]\mathrm{d}z\right)\mathrm{d}\phi \\ C_5 = \frac{N_f}{2\pi}\int_0^{2\pi}\left(\int_{z_2(\phi_j)}^{z_2(\phi_j)}\left[-\frac{1}{2}\ \cos(\kappa(z))\left(1-2\ \cos\left(2\phi_j-2\frac{\tan\beta}{R_0}z\right)\right)\right]\mathrm{d}z\right)\mathrm{d}\phi \\ C_6 = \frac{N_f}{2\pi}\int_0^{2\pi}\left(\int_{z_2(\phi_j)}^{z_2(\phi_j)}\left[-\cos(\kappa(z))\sin\left(\phi_j-\frac{\tan\beta}{R_0}z\right)*M\right]\mathrm{d}z\right)\mathrm{d}\phi \\ C_7 = \frac{N_f}{2\pi}\int_0^{2\pi}\left(\int_{z_2(\phi_j)}^{z_2(\phi_j)}\left[\frac{1}{2}\left(1-2\ \cos\left(2\phi_j-2\frac{\tan\beta}{R_0}z\right)\right)\right]\mathrm{d}z\right)\mathrm{d}\phi \\ C_8 = \frac{N_f}{2\pi}\int_0^{2\pi}\left(\int_{z_2(\phi_j)}^{z_2(\phi_j)}\left[\sin\left(\phi_j-\frac{\tan\beta}{R_0}z\right)*M\right]\mathrm{d}z\right)\mathrm{d}\phi \\ C_9 = \frac{N_f}{2\pi}\int_0^{2\pi}\left(\int_{z_2(\phi_j)}^{z_2(\phi_j)}\left[-\frac{1}{2}\ \sin(\kappa(z))\sin\left(2\phi_j-2\frac{\tan\beta}{R_0}z\right)\right]\mathrm{d}z\right)\mathrm{d}\phi \\ C_{10} = \frac{N_f}{2\pi}\int_0^{2\pi}\left(\int_{z_2(\phi_j)}^{z_2(\phi_j)}\left[-\ \sin(\kappa(z))\cos\left(\phi_j-\frac{\tan\beta}{R_0}z\right)*M\right]\mathrm{d}z\right)\mathrm{d}\phi \\ C_{11} = \frac{N_f}{2\pi}\int_0^{2\pi}\left(\int_{z_2(\phi_j)}^{z_2(\phi_j)}\left[-\frac{1}{2}\ \cos(\kappa(z))\sin\left(2\phi_j-2\frac{\tan\beta}{R_0}z\right)\right]\mathrm{d}z\right)\mathrm{d}\phi \\ C_{12} = \frac{N_f}{2\pi}\int_0^{2\pi}\left(\int_{z_2(\phi_j)}^{z_2(\phi_j)}\left[-\cos(\kappa(z))\cos\left(\phi_j-\frac{\tan\beta}{R_0}z\right)*M\right]\mathrm{d}z\right)\mathrm{d}\phi \\ C_{13} = \frac{N_f}{2\pi}\int_0^{2\pi}\left(\int_{z_2(\phi_j)}^{z_2(\phi_j)}\left[\cos(\kappa(z))\sin\left(\phi_j-\frac{\tan\beta}{R_0}z\right)\right]\mathrm{d}z\right)\mathrm{d}\phi \\ C_{14} = \frac{N_f}{2\pi}\int_0^{2\pi}\left(\int_{z_2(\phi_j)}^{z_2(\phi_j)}[\cos(\kappa(z))*M]\mathrm{d}z\right)\mathrm{d}\phi \\ C_{15} = \frac{N_f}{2\pi}\int_0^{2\pi}\left(\int_{z_2(\phi_j)}^{z_2(\phi_j)}\left[-\ \sin(\kappa(z))\sin\left(\phi_j-\frac{\tan\beta}{R_0}z\right)\right]\mathrm{d}z\right)\mathrm{d}\phi \\ C_{16} = \frac{N_f}{2\pi}\int_0^{2\pi}\left(\int_{z_2(\phi_j)}^{z_2(\phi_j)}[-\ \sin(\kappa(z))*M]\ \mathrm{d}z\right)\mathrm{d}\phi \end{cases} \tag{20}$$

Combining Eqs. (16), (18), (19) and (20), the average cutting forces can be determined by Eq. (21).

$$\begin{cases} \overline{F}_f = (C_1K_{tc} + C_3K_{rc} + C_5K_{ac})f_t + C_2K_{te} + C_4K_{re} + C_6K_{ae} \\ \overline{F}_n = (C_7K_{tc} + C_9K_{rc} + C_{11}K_{ac})f_t + C_8K_{te} + C_{10}K_{re} + C_{12}K_{ae} \\ \overline{F}_a = (C_{13}K_{rc} + C_{15}K_{ac})f_t + C_{14}K_{re} + C_{16}K_{ae} \end{cases} \tag{21}$$

Since the average cutting forces can be expressed as a linear function, as shown in Eq. (22), according the analysis of the experimental data, the relation in Eqs. (23) and (24) can be established.

$$\begin{cases} \overline{F}_f = \overline{F}_{fc}f_t + \overline{F}_{fe} \\ \overline{F}_n = \overline{F}_{nc}f_t + \overline{F}_{ne} \\ \overline{F}_a = \overline{F}_{ac}f_t + \overline{F}_{ae} \end{cases} \tag{22}$$

$$\begin{cases} \overline{F}_f = \overline{F}_{fc}f_t + \overline{F}_{fe} = (C_1K_{tc} + C_3K_{rc} + C_5K_{ac})f_t + C_2K_{te} + C_4K_{re} + C_6K_{ae} \\ \overline{F}_n = \overline{F}_{nc}f_t + \overline{F}_{ne} = (C_7K_{tc} + C_9K_{rc} + C_{11}K_{ac})f_t + C_8K_{te} + C_{10}K_{re} + C_{12}K_{ae} \\ \overline{F}_a = \overline{F}_{ac}f_t + \overline{F}_{ae} = (C_{13}K_{rc} + C_{15}K_{ac})f_t + C_{14}K_{re} + C_{16}K_{ae} \end{cases} \tag{23}$$

$$\begin{cases} \overline{F}_{fc} = C_1K_{tc} + C_3K_{rc} + C_5K_{ac} \\ \overline{F}_{fe} = C_2K_{te} + C_4K_{re} + C_6K_{ae} \\ \overline{F}_{nc} = C_7K_{tc} + C_9K_{rc} + C_{11}K_{ac} \\ \overline{F}_{ne} = C_8K_{te} + C_{10}K_{re} + C_{12}K_{ae} \\ \overline{F}_{ac} = C_{13}K_{rc} + C_{15}K_{ac} \\ \overline{F}_{ae} = C_{14}K_{re} + C_{16}K_{ae} \end{cases} \tag{24}$$

The components of the linear force $\overline{F}_{fc}, \overline{F}_{fe}, \overline{F}_{nc}, \overline{F}_{ne}, \overline{F}_{ac}$, and $\overline{F}_{ae}$ can be calculated by a linear regression of the measured cutting force data. Finally, the cutting force coefficients can be determined by Eq. (25).

$$\Rightarrow \begin{cases} K_{ac} = \frac{\overline{F}_{ac}(C_3C_7C_{15} - C_1C_9C_{15}) - C_7C_{13}C_{15}\overline{F}_{fc} + C_1C_{13}C_{15}\overline{F}_{nc}}{C_3C_7C_{15}^2 - C_5C_7C_{13}C_{15} - C_1C_9C_{15}^2 + C_1C_{11}C_{13}C_{15}} \\ K_{ae} = \frac{\overline{F}_{ae}(C_4C_8C_{16} - C_2C_{10}C_{16}) - C_{14}C_8C_{16}\overline{F}_{fe} + C_2C_{14}C_{16}\overline{F}_{ne}}{C_4C_8C_{16}^2 - C_6C_8C_{14}C_{16} - C_2C_{10}C_{16}^2 + C_2C_{12}C_{14}C_{16}} \\ K_{rc} = \frac{C_7C_{15}\overline{F}_{fc} - C_1C_{15}\overline{F}_{nc} + (C_1C_{11} - C_5C_7)\overline{F}_{ac}}{C_3C_7C_{15} - C_5C_7C_{13} - C_1C_9C_{15} + C_1C_{11}C_{13}} \\ K_{re} = \frac{C_8C_{16}\overline{F}_{fe} - C_2C_{16}\overline{F}_{ne} + (C_2C_{12} - C_8C_6)\overline{F}_{ae}}{C_4C_8C_{16} - C_6C_8C_{14} - C_2C_{10}C_{16} + C_2C_{12}C_{14}} \\ K_{tc} = \frac{\overline{F}_{fc} - C_3K_{rc} - C_5K_{ac}}{C_1} \\ K_{te} = \frac{\overline{F}_{fe} - C_4K_{re} - C_6K_{ae}}{C_2} \end{cases} \tag{25}$$

3. Experimental work

3.1. Experimental procedure

The research procedure was performed sequentially as shown in Fig. 3. First, the stability lobe diagram was measured by the CUTPRO™ software. By this work, the cutting depths and spindle speeds were selected in the stable zone of the stability lobe diagram to avoid the chatter and to reduce the vibrations. Next, the cutting tests were conducted to determine the cutting force coefficients. And then, the cutting force coefficients were calculated from the experimental data, and the cutting forces were simulated by using the calculated cutting force coefficients. Finally, the simulated cutting forces were verified by the experimental results.

3.2. Setup of the experiment

The setup of the experiments in this paper includes workpiece and tool, machine tool dynamic measurement and cutting force measurement. The description of the setup is as the followings:

3.2.1. Workpiece, tool, and CNC machine

A series of end milling experiments were performed. The cutter was chosen as follows. Cutter: a HSS-Co ball-end mill with number of flutes $N_f=2$, helix angle $\beta=30^\circ$, rake angle $\alpha_r=5^\circ$, and the diameter was 8 mm.

The workpiece material was grey cast iron FC25 (Ferrum Casting). The compositions of grey cast iron FC25 are listed in Table 1 and the properties of the FC25 were: hardness 197–269 HB, Young's modulus = 109.5 GPa, Poisson's ratio = 0.29, tensile strength = 250 MPa. The experiments were performed at a Three-axis Vertical Milling Center (Tongtai TMV-720 A).

3.2.2. Setup for determination of stable cutting conditions

An integrated measurement system that consisted of the acceleration sensor (ENDEVCO-25B-10668), hammer (KISTLER-9722A2000), signal processing box (NI 9234), and CUTPRO^{TM} software was used to analyze the stability lobe. The detail settings of the measurement experiment are illustrated in Fig. 4. The spindle speed and axial depth of cut in the stable zone were chosen according to the stability lobe diagram measured by CUTPRO^{TM} software as shown in Fig. 5.

3.2.3. Setup and measurement of cutting forces

A dynamometer (type XYZ FORCE SENSOR, model 624-120-5KN), processing system, and a PC were used to measure cutting forces. The detail is illustrated in Fig. 6. At each depth of cut, full immersion (slotting) experiments were repeated in every feed per flute. The spindle speed was held constant at each experiment. The experiments were performed with the different parameters, as shown in Table 2.

4. Experimental results and discussions

4.1. The suitable machining conditions for determination of cutting force coefficients

In order to avoid the chatter and reduce the vibration, the stable cutting conditions were determined. By using the measured results of the frequency response function of the machine tool dynamic system, the stability lobes were analyzed by CUTPRO^{TM} software and described in Fig. 5. The stable cutting conditions (axial depth of cut and spindle speed) were chosen at the stable zone of the stability lobe diagram.

The analyzed results show that the machining processing is stable at the depth of cut less than 0.6 mm, and at all range spindle speeds. In this zone, the chatter was prevented for all cutting tests. Besides, using the experimental method as detailed in Ref. [19],

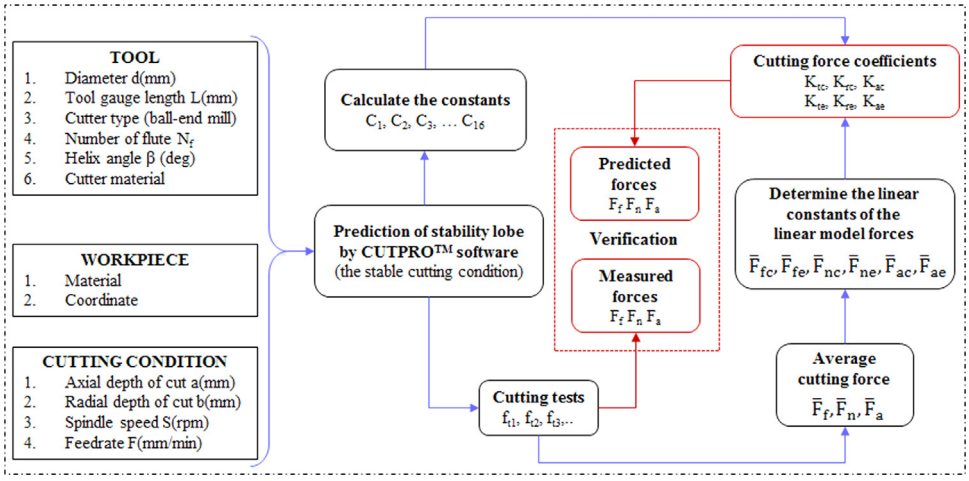

Fig. 3. Approach to determine cutting force coefficients and to predict the cutting forces.

Table 1
Chemical compositions of grey cast iron FC25.

Composite (%)						
	C	Mn	Si	P	S	Fe
Min	2.44	0.39	1.83	0.15	–	
Max	3.02	0.52	2.03	0.30	0.15	Balance

several trial cutting tests were performed in the stable zone of the stability lobe diagram. Finally, the axial depth of cut and the spindle speed were chosen, as listed in Table 2, to avoid the chatter and to reduce the machine tool vibrations.

4.2. Verification of the linear model of average cutting forces

The cutting tests were performed at stable cutting conditions as listed in Table 2. For each experiment, the average cutting force in feed, normal, and axial directions were calculated from the measured cutting force data. The relationship of the average cutting force and the feed per tooth was estimated and illustrated in Fig. 7. In this figure, all the absolute values of average cutting forces increase with the increases of feed per flute. This experimental result is reasonable with the theory of cutting force model because when the feed per flute increases, the chip thickness increases. The increase of chip thickness make the cutting force's amplitude increases, and finally, the absolute value of average cutting force increases. This results show that the theory results and experimental results have good agreement, and the relationship of average cutting forces and feed per flute was characterized as a linear function. Therefore, in ball-end mill with stable cutting condition (no chatter and very small vibration, etc.), the measured average cutting force can be expressed by the linear function of feed per flute and the measured data can be used to estimate the

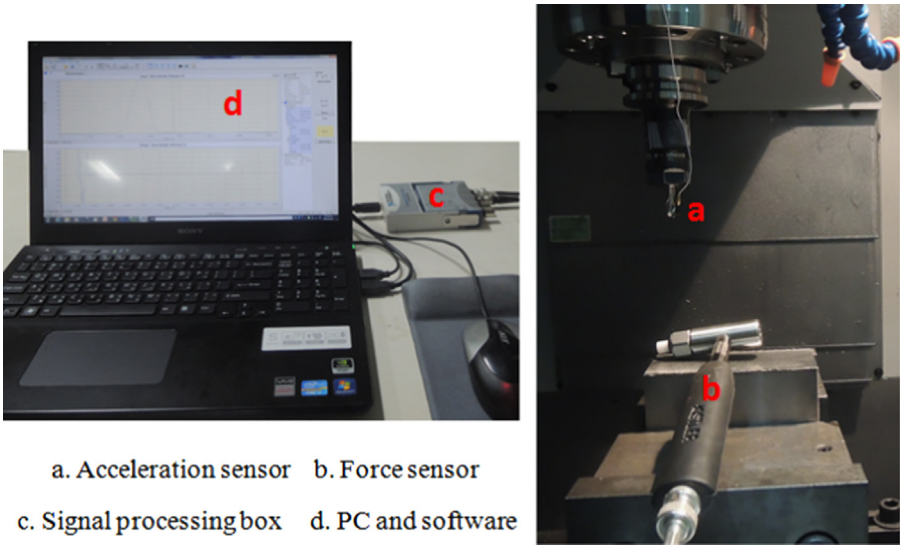

Fig. 4. Setup of experiment for analytical stability lobes.

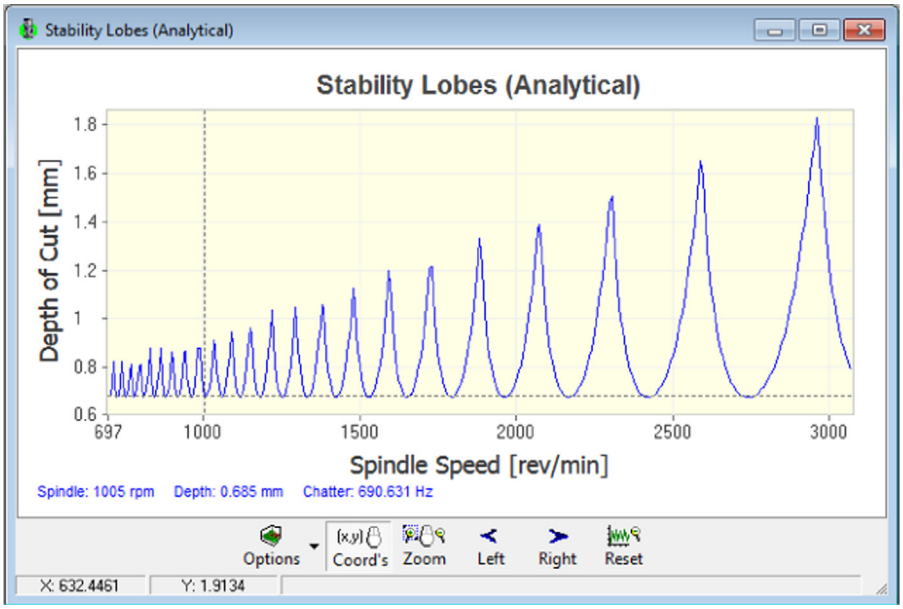

Fig. 5. The stability lobe diagram of the adopted CNC machine.

Fig. 6. Setup measurement of cutting force setting.

Table 2
The stable machining conditions.

Test No	Tool diameter [mm]	Number of flutes	Helix angle [deg]	Axial depth of cut [mm]	Feed per flute [mm/flute]	Spindle speed [rpm]
1	8	2	30	0.2	0.050	1000
2	8	2	30	0.2	0.075	1000
3	8	2	30	0.2	0.100	1000
4	8	2	30	0.2	0.125	1000
5	8	2	30	0.2	0.150	1000

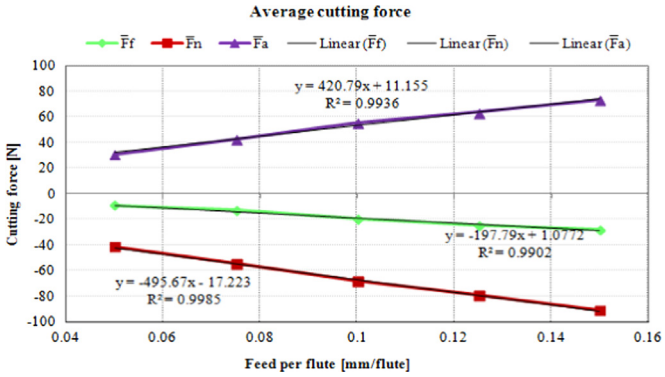

Fig. 7. The average cutting forces versus feed per flute.

cutting force coefficients for each pair of cutter and workpiece. By this method, all cutting force coefficient components were determined.

Using Fitting Toolbox of MATLAB™ and linear regression, the best lines passing through the values of average cutting force was determined. By using the characteristic of the best line and the formula of cutting force coefficients, the cutting force coefficients were calculated and listed in Table 3.

4.3. Verification of simulation results

Using the calculated cutting force coefficients in Table 3, the cutting forces were predicted and compared with the measured results as shown in Fig. 8 to Fig. 10. The difference of the amplitudes of predicted and measured forces were investigated. The research results showed that the predicted cutting forces have some differences to the measured cutting forces. In the milling

Table 3
Prediction of cutting force coefficients.

Shearing force coefficient [N/mm²]			Edge force coefficient [N/mm]		
K_{tc}	K_{rc}	K_{ac}	K_{te}	K_{re}	K_{ae}
3304.12	2148.90	725.07	67.58	5.25	−7.16

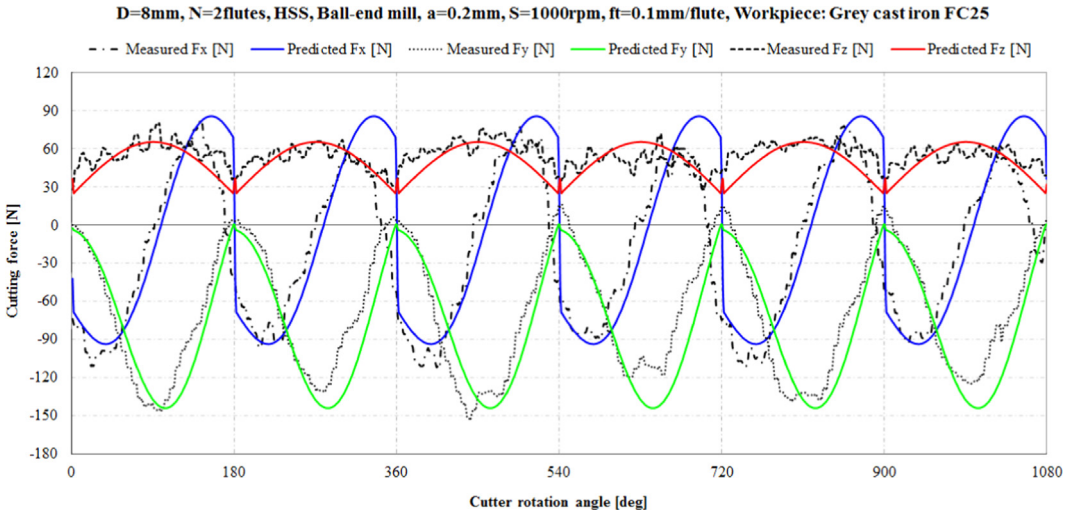

Fig. 8. Comparison between measured and predicted forces with small depth of cut and low spindle speed.

processes with low spindle speed as described in Fig. 8 and Fig. 9 ($S = 1000$ rpm), the shape of measured and predicted force are very similar to each other. About the amplitude of cutting force, the differences are about 6.9% in feed direction, 8.5% in normal direction, and 17% in axial direction. The difference is small because when milling with low spindle speed, the effect of vibrations on cutting process is quite small; so, the cutting process is close to the static cutting, and then the predicted cutting force is close to the measured cutting force.

In the milling process with higher spindle speed (3000 rpm), by the effect of machine tool dynamic structure on the milling process, vibrations increase. When the vibrations increase, the chip thickness changes in each flute, it makes the cutting forces in each flute different at the same position but in different revolution. The differences between measured forces and predicted cutting force are described as in Fig. 10. This figure showed that the shapes of predicted and measured cutting forces are similar to each other, the peaks of predicted and measured cutting force sometimes are the same, sometimes are different. About the amplitudes of cutting force, the differences are about 14.5% in feed direction, 23% in normal direction and about 30% in axial direction. So, when the spindle speed increases the difference of cutting force amplitudes between measured and predicted cutting force increases. These differences can be explained when applying the machine tool dynamic process in milling process that will be investigated in the future study.

The analyzed results showed that the predicted result of research model coincides roughly with the measured one. Therefore, the predicted results from research model agree satisfactorily with experimental results and the cutting force models and cutting force coefficient models in this study are good models that can be used to determine the cutting force coefficients in the milling processes.

The reasons for the above differences were mostly originated from the changes of tool geometry following the tool tip up, the noise, the vibrations, the deflections, the inconstancy of cutting depth, the inhomogeneous distribution of tool and workpiece hardness, the temperature, the friction, and so on.

5. Conclusions

In this study, the developed model was used to analyze the theory of the cutting force in the ball-end mill processes. By mathematical derivation, a combined theoretical–experimental method was improved and an effective model was proposed for the determination of cutting force coefficients. This method could be applied in the stable cutting condition when the machine tool vibration is small and the effects of other subordinate factors are limited.

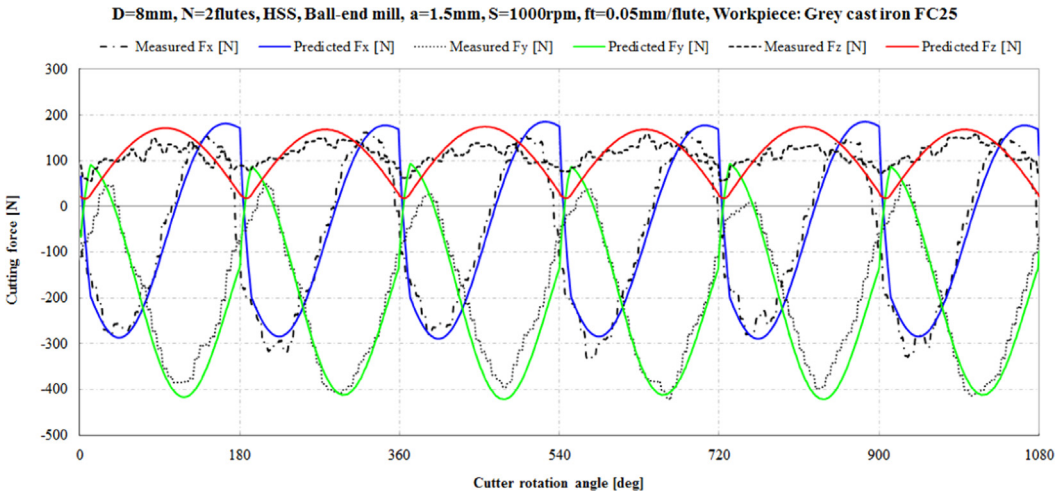

Fig. 9. Comparison between measured and predicted forces with large depth of cut and low spindle speed.

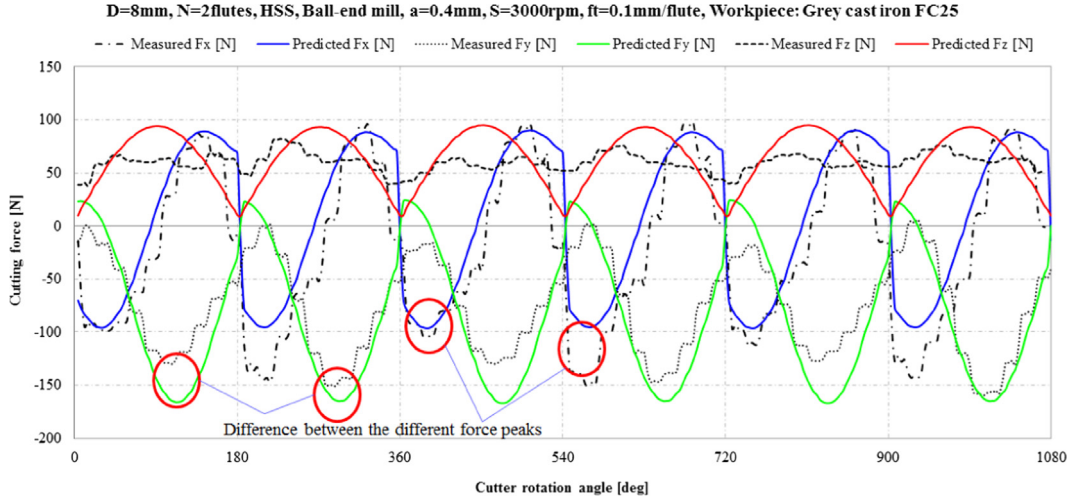

Fig. 10. Comparison between measured and predicted forces with high spindle speed.

An experimental method was proposed to determine the stable cutting condition in milling processes. By using this method, the chatter was prevented, and the vibration of machine tool was reduced in the milling process.

In the stable cutting condition, the relationship between the average cutting forces and the feed per flute could be expressed by a linear function. This relationship was successfully used to determine the cutting force coefficients in the ball-end mill processes. The determined cutting force coefficients and the force models have been successfully verified by both simulation and experiment with very promising results. By the proposed model in this paper, all cutting force coefficients were determined by experimental data.

This research model is expected to be extended to more complex type of milling tool such as bull-end mill, general-end mill, and so on. The application of dynamic process in milling simulation should be used to analyze the dynamic cutting force, and that will be the futuristic study of the extended research.

Acknowledgments

The authors appreciate the support of the Ministry of Science and Technology, Taiwan (MOST) from the grant MOST 103-2218-E-194-005-MY2 and the generous assistance from the High Speed Machining Lab for the dynamometer in the cutting forces measurement experiments. Thanks also extend to the support from the Advanced Institute of Manufacturing with High-tech Innovations, National Chung Cheng University, Taiwan.

Appendix

The instantaneous chip thickness $h_j(\phi_j(z))$ is determined by Eq. (A.1).

$$h_j\left(\phi_j(z)\right) = f_t \sin\left(\phi_j(z)\right) \sin\left(\kappa(z)\right) \tag{A.1}$$

where $\kappa(z)$ is the axial immersion angle at z axial depth of cut.so,

$$\begin{cases} \sin(\kappa(z)) = \frac{r(\phi_j(z))}{R_0} \\ \cos(\kappa(z)) = \frac{(R_0 - z)}{R_0} \end{cases} \tag{A.2}$$

where $r(\phi_j(z))$ is the radius of a circle on xy plane at an arbitrary point (P) on cutting edge; so, $r(\phi_j(z))$ can be determined by Eq. (A.3)

$$r(\phi_j(z)) = \sqrt{R_0^2 - (R_0 - z)^2} \tag{A.3}$$

so,

$$\Rightarrow \quad \sin(\kappa(z)) = \frac{\sqrt{R_0^2 - (R_0 - z)^2}}{R_0} \tag{A.4}$$

The static chip thickness is calculated by Eq. (A.1); so, it can be calculated by Eq. (A.5).

$$h_j(\phi_j(z)) = f_t \frac{\sqrt{R_0^2 - (R_0 - z)^2}}{R_0} \sin\left(\phi_j - \frac{\tan\beta}{R_0} z\right) \tag{A.5}$$

The chip width is calculated by Eqs. (A.6) and (A.7)

$$\mathrm{db} = \frac{\mathrm{d}z}{\sin(\kappa(z))} \tag{A.6}$$

so,

$$\Rightarrow \mathrm{db} = \frac{R_0}{\sqrt{R_0^2 - (R_0 - z)^2}} \mathrm{d}z \tag{A.7}$$

The edge length of the cutting segment dS is obtained by the small variation of a vector, which is obtained from the point center (C) to a point (P) on the cutting edge, with respect to the small variation of rotation angle (ϕ). The location of P on the flute number j is defined by a vector in cylindrical coordinates as described in Fig. 2 and can be expressed by Eq. (A.8).

$$\vec{r}(\phi_j(z)) = r(\phi_j(z)) \sin(\phi_j(z)) * \vec{i} + r(\phi_j(z)) \cos(\phi_j(z)) * \vec{j} + z * \vec{k} \tag{A.8}$$

where z is the z coordinate of point P.

so, dS can be derived by Eqs. (A.9) and (A.10).

$$\mathrm{dS} = \left|\mathrm{d}\vec{r}(\phi_j, z)\right| = \sqrt{\left\{\left[r((\phi_j, z) \sin(\phi_j(z))\right]'\right\}^2 + \left\{\left[r(\phi_j(z)) \cos(\phi_j(z))\right]'\right\}^2 + \left\{[z]'\right\}^2} \tag{A.9}$$

$$\Rightarrow \mathrm{dS} = \mathrm{d}z \sqrt{\frac{(R_0 - z)^2}{R_0^2 - (R_0 - z)^2} + \frac{\tan^2\beta}{R_0^2}\left[R_0^2 - (R_0 - z)^2\right] + 1} = M\mathrm{d}z \tag{A.10}$$

with

$$M = \sqrt{\frac{(R_0 - z)^2}{R_0^2 - (R_0 - z)^2} + \frac{\tan^2\beta}{R_0^2}\left[R_0^2 - (R_0 - z)^2\right] + 1} \tag{A.11}$$

The components of cutting forces can be calculated by Eq. (A.12).

$$\begin{cases} \mathrm{d}F_{t,j}(\phi_j(z)) = K_{tc} * f_t \frac{\sqrt{R_0^2 - (R_0 - z)^2}}{R_0} \sin\left(\phi_j - \frac{\tan\beta}{R_0} z\right) * \frac{R_0}{\sqrt{R_0^2 - (R_0 - z)^2}} dz + K_{te} * M\mathrm{d}z \\ \mathrm{d}F_{r,j}(\phi_j(z)) = K_{rc} * f_t \frac{\sqrt{R_0^2 - (R_0 - z)^2}}{R_0} \sin\left(\phi_j - \frac{\tan\beta}{R_0} z\right) * \frac{R_0}{\sqrt{R_0^2 - (R_0 - z)^2}} dz + K_{re} * M\mathrm{d}z \\ \mathrm{d}F_{a,j}(\phi_j(z)) = K_{ac} * f_t \frac{\sqrt{R_0^2 - (R_0 - z)^2}}{R_0} \sin\left(\phi_j - \frac{\tan\beta}{R_0} z\right) * \frac{R_0}{\sqrt{R_0^2 - (R_0 - z)^2}} dz + K_{ae} * M\mathrm{d}z \end{cases} \tag{A.12}$$

So,

$$\begin{cases} dF_{t,j}(\phi_j(z)) = \left[K_{tc} * f_t \ \sin\left(\phi_j - \frac{\tan\beta}{R_0} z\right) + K_{te} * M\right] dz \\ dF_{r,j}(\phi_j(z)) = \left[K_{rc} * f_t \ \sin\left(\phi_j - \frac{\tan\beta}{R_0} z\right) + K_{re} * M\right] dz \\ dF_{a,j}(\phi_j(z)) = \left[K_{ac} * f_t \ \sin\left(\phi_j - \frac{\tan\beta}{R_0} z\right) + K_{ae} * M\right] dz \end{cases} \quad (A.13)$$

References

[1] Merchant ME. Mechanics of the metal cutting process. I. Orthogonal cutting and a type 2 chip. *J. Appl. Phys.* 1945;**16**: 267. http://dx.doi.org/10.1063/1.1707586.

[2] Altintas Y. *Manufacturing Automation: Metal Cutting Mechanics, Machine Tool Vibrations, and CNC Design*, 2nd ed., New York: Cambridge University Press; 2012. ISBN 978-1-00148-0.

[3] Budak E, Altintas Y, Armarego EJA. Prediction of milling force coefficients from orthogonal cutting data. *ASME J. Manuf. Sci. Eng.* 1996;**118**:216–24.

[4] Sonawane HA, Joshi SS. Analytical modeling of chip geometry and cutting forces in helical ball end milling of superalloy Inconel 718. *CIRP J. Manuf. Sci. Technol.* 2010;**3**:204–17.

[5] Yang M, Park H. The prediction of cutting force in ball-end milling. *Int. J. Mach. Tools Manuf.* 1991;**31**:45–54.

[6] Lee P, Altintas Y. Prediction of ball-end milling forces from orthogonal cutting data. *Int. J. Mach. Tools Manuf.* 1996;**36**:1059–72.

[7] Budak E, Ozturk E, Tunc LT. Modeling and simulation of 5-axis milling processes. *CIRP Ann. Manuf. Technol.* 2009;**58**(1)347–50.

[8] Cheng PJ, Tsay JT, Lin SC. A study on instantaneous cutting force coefficients in face milling. *Int. J. Mach. Tools Manuf.* 1997;**37**:1393–408.

[9] Bayoumi AE, Yucesan G, Kendall LA. An analytic mechanistic cutting force model for milling operations: a theory and methodology. *Trans. ASME J. Eng. Ind.* 1994;**116**:324–30.

[10] Shin YC, Waters AJ. A new procedure to determine instantaneous cutting force coefficients for machining force prediction. *Int. J. Mach. Tools Manuf.* 1997;**37**:1337–51.

[11] Larue A, Anselmetti B. Deviation of a machined surface in flank milling. *Int. J. Mach. Tools Manuf.* 2003;**43**:129–38.

[12] Ko JH, Cho DW. Determination of cutting-condition-independent coefficients and runout parameters in ball-end milling. *Int. J. Adv. Manuf. Technol.* 2005;**26**: 1211–21.

[13] Subrahmanyam KVR, San WY, Soon HG, Sheng H. Cutting force prediction for ball nose milling of inclined surface. *Int. J. Adv. Manuf. Technol.* 2010;**48**: 23–32.

[14] Altintas Y. Modeling approaches and software for predicting the performance of milling operations at MAL-UBC. *Int J. Mach. Sci. Technol.* 2000;**4**(3) 445–78.

[15] Budak E. Analytical models for high performance milling. Part I: cutting forces, structural deformations and tolerance integrity. *Int. J. Mach. Tools Manuf.* 2006;**46**:1478–88.

[16] Adetoro OB, Wen PH. Prediction of mechanistic cutting force coefficients using ALE formulation. *Int. J. Adv. Manuf. Technol.* 2010;**46**:79–90.

[17] Wang M, Gao L, Zheng Y. An examination of the fundamental mechanics of cutting force coefficients. *Int. J. Mach. Tools Manuf.* 2014;**78**:1–7.

[18] Liu XW, Cheng K, Webb D, Luo XC. Improved dynamic cutting force model in peripheral milling. Part I: theoretical model and simulation. *Int. J. Adv. Manuf. Technol.* 2002;**20**:631–8.

[19] Kao YC, Nguyen NT, Chen MS, Su ST. A prediction method of cutting force coefficients with helix angle of flat-end cutter and its application in a virtual three-axis milling simulation system. *Int. J. Adv. Manuf. Technol.* 2015;**77**(9–12)1793–809.

[20] Narita H. A determination method of cutting coefficients in ball end milling forces model. *Int. J. Autom. Technol.* 2013;**7**(1)39–44.

[21] Gao G, Wu B, Zhang D, Luo M. Mechanistic identification of cutting force coefficients in bull-nose milling process. *Chin. J. Aeronaut.* 2013;**26**(3)823–30.